Solving the Paradox of the Inconsistent Size Dependence of Thermal Stability at Device and Chip-level in Perpendicular STT-MRAM

Luc Thomas, Guenole Jan, Son Le, Yuan-Jen Lee, Huanlong Liu, Jian Zhu, Santiago Serrano-Guisan, Ru-Ying Tong, Keyu Pi, Dongna Shen, Renren He, Jesmin Haq, Zhongjian Teng, Rao Annapragada, Vinh Lam, Yu-Jen Wang, Tom Zhong, Terry Torng and Po-Kang Wang.

TDK- Headway Technologies, 463 S. Milpitas Boulevard, Milpitas CA 95035, USA
Tel: (408) 935-1338, Fax: (408) 935-1393, Email: luc.thomas@headway.com

Abstract

Current understanding of thermal stability of perpendicular STT-MRAM based on device-level data suggests that the thermal stability factor Δ is almost independent of device diameter above ~30nm. Here we report that contrary to this conventional wisdom, chip-level data retention exhibits substantial size dependence for diameters between 55 and 100 nm. We show that the method widely used to measure Δ is inaccurate for devices larger than ~30 nm, leading to significant underestimation of the size dependence. We derive an improved model, allowing us to reconcile the size dependence of Δ measured at device and chip level.

Introduction

The combination of high-speed and non-volatility of perpendicular Spin-Transfer-Torque Magnetic Random Access Memories (pSTT-MRAMs) promises a significant reduction of computing power, making this technology particularly suited for embedded memory applications [1]. However, despite the importance of data retention for applications, thermal stability of pSTT-MRAMs is poorly understood. Device-level data reported in the literature suggest that Δ is almost independent of diameter above ~30nm [2-5]. By contrast, we find that chip-level data retention exhibits significant size dependence between 55 and 100 nm. We show that both device and chip-level data are well described by a domain-wall (DW) mediated magnetization reversal model, for which Δ varies almost linearly with diameter [3, 6]. Our results suggest that the lack of size dependence of Δ reported in the literature is an artifact of fitting data to a model inaccurate for diameters > ~30nm. Actual values of Δ are much larger than those derived using the conventional method (more than 2x at 70 nm diameter).

Chip-level Data Retention

Data retention was measured as a function of time and temperature on 8 Mbits arrays of devices having diameters between 55 and 100 nm [5, 7]. Fig. 1 shows a cross-sectional TEM image of a typical device. Fig. 2 shows a schematic of the energy barrier separating the low (‘0’) and high resistance (‘1’) logic states. Devices are reset in equal numbers in each state prior to each experiment. Fig. 3 shows the error rate in both ‘0’ and ‘1’ state versus time at 216.5°C for 55nm devices. Data are well fitted to a Néel-Brown relaxation model including bidirectional relaxation and Gaussian distributions of Δ in both states [8, 9]. Best fitting parameters are indicated in the figure. The width of the distribution is 8.6 and 9.8% in the ‘0’ and ‘1’ state, respectively. We have reported recently that at low error rate, the properties of a distribution of devices centered on Δ_m with a width σ are the same as those of a set of identical devices having an effective thermal stability factor $\Delta_{eff} = \Delta_m - \sigma^2/2$ [9]. Δ_{eff} can be derived directly from the data: $\Delta_{eff} = \ln(f_a t/P)$, where f_a = 1GHz is the attempt frequency, t the bake time and P the error rate. Fig. 4 shows Δ_{eff} versus temperature for various device diameters. Data vary linearly with temperature for all sizes. The slope increases with device diameter from 0.24 at 55 nm to 0.36 at 100 nm. The size dependence of Δ_{eff} extrapolated from these linear fits is shown in Fig. 5 at indicated temperatures. Data are well described by a power law with an exponent of 0.67. From these data, arrays of 60 nm devices exceed 10 year data retention (corresponding to Δ_{eff} =54) up to 125°C.

Device-level Thermal Stability Factor

In most reports, Δ is derived from the field dependence of the switching probability $P_{SW}(H) = 1 - exp(-f_a t exp(-\Delta(H)))$ where t ~ 0.1sec is the time scale of the magnetic field application [3-5]. Zero-field values are extrapolated using the Stoner-Wolfarth model of uniform magnetization reversal for which $\Delta(H) = \Delta(1-H/H_K)^2$, where H_K is the anisotropy field. Examples of experimental data and fits to this model are shown in Fig. 6 as symbols and solid lines, respectively. Zero-field values of Δ extrapolated from these fits are shown as solid blue squares in Fig. 7. Δ is almost independent on diameter, in agreement with published data [2-5]. However, micromagnetic simulations show that DW-mediated magnetization reversal is energetically favorable down to diameters of ~40nm [3]. Fig. 8 shows the energy versus magnetization of an 80 nm device for both uniform and DW reversals. The energy barrier is more than two times smaller in the latter case. As shown in Fig. 9, the field dependence of Δ derived from these energy profiles is very different for DW and uniform reversal mechanisms. In experiments, P_{sw} is measured close to the coercive field $H=H_C$, corresponding to $\Delta(H_C)$~20 (Fig. 10). Thus, the value of Δ extrapolated to H=0 using the uniform reversal model is significantly underestimated compared to the actual value for DW reversal (Fig. 11). In the following, we show that this underestimation

in the extrapolation of Δ may explain the apparent lack of size dependence in Fig. 7 and in [2-5].

Domain-Wall Mediated Reversal Model

We develop an analytical model based on DW propagation in circular devices similar to that described in [10] for square shaped devices. The magnetic free energy of the device E_{mag} is composed of three terms: (1) DW energy proportional to the DW energy density σ_W and the DW length l_w (2) Zeeman energy of the reversed domain of area A (3) Zeeman energy of the non-reversed domain πR^2-A. Note that the magnetostatic energy is included in the effective anisotropy constant $K_{eff}=K-2\pi N M_S^2$ where N is the demagnetizing factor of the disk-shaped device having radius R and thickness t and M_S the saturation magnetization. The magnetic energy for an applied field H>0 is written:

$$E_{mag} = (\pi R^2 - A)M_S Ht - AM_S Ht + \sigma_W l_W t \qquad (1)$$

Micromagnetic simulations show that A and l_w are defined by the intersection of the circular device with a virtual circle of radius r centered at distance d from the center of the device (see Fig. 12). The expressions of A and l_w are as follows:

$$A = r^2 cos^{-1}\left(\frac{r^2+d^2-R^2}{2dr}\right) + R^2 cos^{-1}\left(\frac{R^2+d^2-r^2}{2dR}\right) - \frac{1}{2}\sqrt{(-d+r+R)(d+r-R)(d-r+R)(d+r+R)}$$

$$l_W = 2r sin^{-1}\sqrt{1-\left(\frac{d^2+r^2-R^2}{2dr}\right)^2}$$

The energy barrier is given by the value of $E_{mag}(r,d)$ at the saddle point defined by:

$$\frac{\partial E_{mag}}{\partial r} = \frac{\partial E_{mag}}{\partial d} = 0 \quad \text{and} \quad \frac{\partial^2 E_{mag}}{\partial r^2}\frac{\partial^2 E_{mag}}{\partial d^2} - \frac{\partial^2 E_{mag}}{\partial r \partial d} < 0$$

Although the analytical derivation is cumbersome, we note from micromagnetic simulations and from numerical calculations of $E_{mag}(r,d)$ that the saddle point corresponds to the case of orthogonal intersecting circles for which $d^2=R^2+r^2$. Using this condition, A and l_w can be simplified:

$$A = r\left(\frac{\pi}{2}r - R\right) + (R^2 - r^2)tan^{-1}\left(\frac{r}{R}\right)$$

$$l_W = \pi r - 2r tan^{-1}\left(\frac{r}{R}\right)$$

The energy barrier is obtained for $r=r_0$ such that $\frac{\partial E_{mag}}{\partial r} = 0$.

It follows that $r_0=\sigma_W/(2M_S H)$. The energy barrier is given by:

$$\begin{aligned}\Delta E &= E_{mag}(r_0) - E_{mag}(0) = -2A(r_0)M_S Ht + \sigma_W l_W(r_0)t \\ &= \sigma_W Rt + \frac{\sigma_W^2 t}{2M_S H}\left(\frac{\pi}{2} - tan^{-1}\left(\frac{\sigma_W}{2M_S HR}\right)\right) \\ &\quad - 2M_S HtR^2 tan^{-1}\left(\frac{\sigma_W}{2M_S HR}\right)\end{aligned}$$

For H→0, ΔE can be expressed as:

$$\Delta E(H \to 0) = 2\sigma_W Rt - M_S HV\left(1 - \frac{4M_S HR}{\pi\sigma_W}\right)$$

where the volume of the device is $V=\pi R^2 t$. The constant term is the energy of the DW located on a diameter of the device, as expected by symmetry for H=0. The first order term H is simply the sum of the Zeeman energy terms for the two halves of the MTJ magnetized parallel and antiparallel to the field. The limit H → ∞ is written as:

$$\Delta E(H \to \infty) = \frac{\pi \sigma_W{}^2 t}{4M_S H}$$

ΔE approaches 0 asymptotically, in contrast with the uniform magnetization reversal model, for which ΔE=0 when $H=H_k$. This is because the DW is infinitely abrupt in the derivation described above. Since in reality, the DW has a finite width, the magnetization within the DW is partially in plane and therefore has a smaller Zeeman contribution than the reversed and non-reversed domains. To account for this, we define a length 2δ within which the Zeeman contribution is zero. With this approximation, the magnetic energy becomes:

$$E_{mag} = (\pi R^2 - A(r+\delta))M_S Ht - A(r-\delta)M_S Ht + \sigma_W l_W t \ (2)$$

By comparing the difference in Zeeman energy integrated between two domains delimited by an abrupt wall or by a Bloch wall of width δ_w, we find $\delta = \delta_w \ln 2$.

$P_{sw}(H)$ data are well fitted using (2) in a wide range of sizes (green solid lines in Fig. 6). Values of Δ extracted from these fits increase almost linearly with diameter (red circles in Fig. 7). By contrast, Δ_{eff} derived from chip-level measurements is sub-linear. The discrepancy is due to the width of the Δ distribution. Fig. 13 shows device-level Δ_m measured at 125°C compared to chip-level Δ_{eff} extrapolated to this same temperature. The difference can be accounted for when the width of the distribution is ~8 to 9% (Fig. 14), in good agreement with the fits of Fig. 3.

Conclusion

Our results show that data retention of pSTT-MRAM chips exhibit significant size dependence for devices between 55 and 100 nm, contrary to published device-level results. Both chip and device-level data are consistent with a domain wall mediated reversal mechanism. The median thermal stability factor Δ varies linearly with size, whereas the effective thermal stability factor Δ_{eff} is sub-linear due to the effect of distributions on chip properties. This size dependence can be leveraged in the design of pSTT-MRAM for non-volatile memory applications.

References

[1] S. H. Kang, Dig. Tech. Pap., Symp. VLSI Technology, **2014**, p36.
[2] J. Z. Sun et al, Phys. Rev B 84, 064413 (2011).
[3] H. Sato et al., Appl. Phys. Lett. **99**, 042501 (2011).
[4] S. Ikeda *et al*., Tech. Dig. - Int. Electron Devices Meet. **2014**, p 796.
[5] L. Thomas *et al*., J. Appl. Phys. **115**, 172615 (2014).
[6] I. Tudosa Appl. Phys. Lett. **100**, 102401 (2012).
[7] G. Jan *et al*., Dig. Tech. Pap., Symp. VLSI Technology, **2014**, p. 42.
[8] K. Tsunoda *et al*., Tech. Dig. - Int. Electron Devices Meet. **2014**, p 486.
[9] L. Thomas *et al*., App. Phys. Lett. **106**, 162402 (2015).
[10] G. D. Chavez-O'Flynn *et al*., J. Appl. Phys. **115**, 172615 (2014).

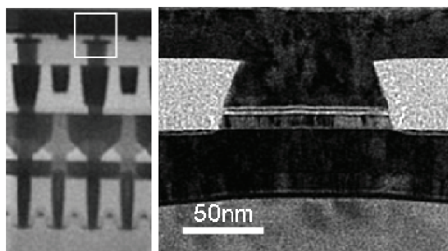

Figure 1. (a) Cross sectional TEM of the test array and (b) a typical pSTT-MRAM device, which is based on CoFeB/MgO/CoFeB/MgO magnetic tunnel junctions.

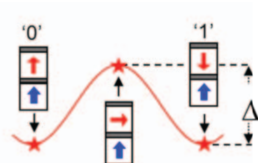

Fig. 2. Schematic of energy barrier separating the '0' and '1'logic state.

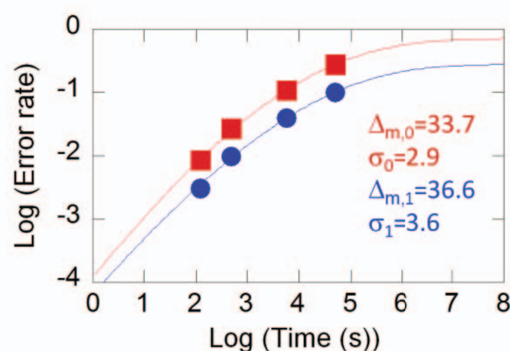

Fig. 3. Error rate vs. time at 216.5C for an array of devices having 55 nm median electrical diameter. Solid symbols and lines show data and fits to the Neel-Brown model, respectively. Data in '0'and '1' states are shown as red squares and blue circles, respectively. Best fits of the mean and width of the distributions of Δ are shown in inset.

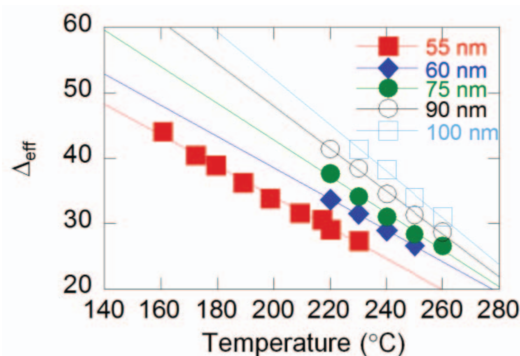

Fig. 4. Effective thermal stability factor versus temperature derived from chip-level data retention experiments for device diameters indicated in the figure. Solid lines are linear fits.

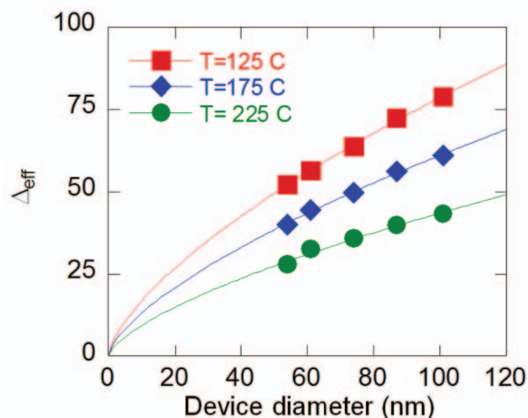

Fig. 5. Δ_{eff} versus electrical device diameter at temperatures indicated on the figure derived from the data shown in Fig. 4. Solid lines show fits to a power law with an exponent of 0.67.

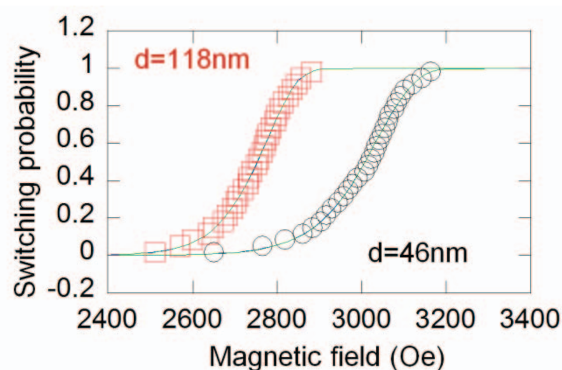

Fig. 6. Device-level switching probability measured at room temperature on two devices. Fits to the uniform and DW reversal models are shown as blue and green solid lines. They overlap almost exactly and cannot be distinguished in the figure.

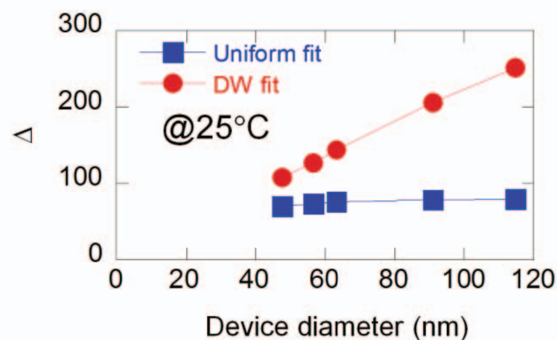

Fig. 7. Δ at room temperature derived from switching probability experiments at device level using models of uniform or DW-mediated magnetization reversal.

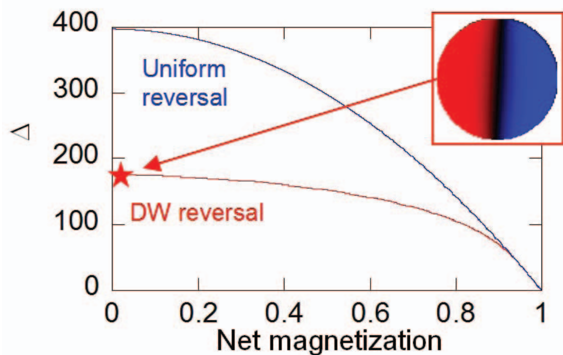

Fig. 8. Δ *vs.* net magnetization calculated by micromagnetic simulations at H=0 for an 80 nm device, for both uniform and DW reversal mechanisms. The magnetization configuration at maximum Δ is shown in inset for the DW reversal. Blue and red colors show regions where the magnetization points out of or into the plane of the device, respectively.

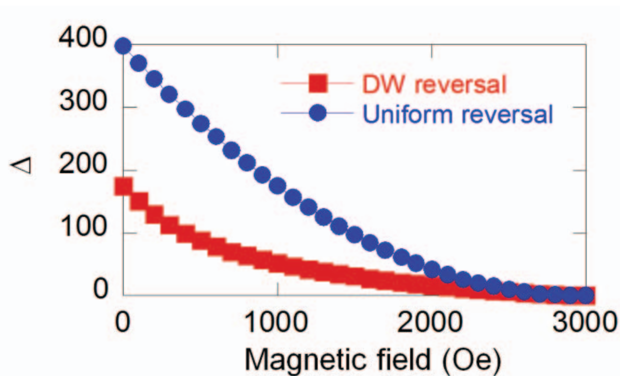

Fig. 9. Dependence of Δ on magnetic field for uniform and DW reversal mechanisms derived from the micromagnetic simulations of an 80 nm device shown in Fig. 8.

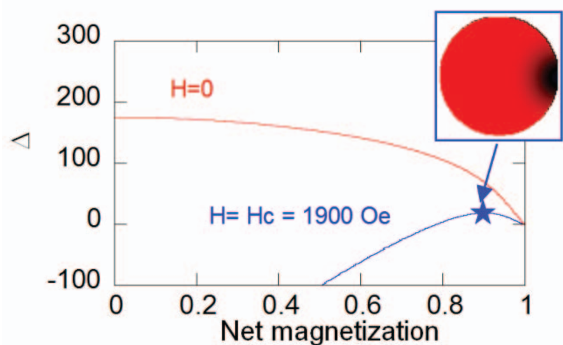

Fig. 10. Δ *vs.* net magnetization calculated by micromagnetic simulations at H=0 and at the coercive field Hc of the 80 nm device (corresponding to an energy barrier Δ~20). The inset shows the magnetization configuration at H=Hc.

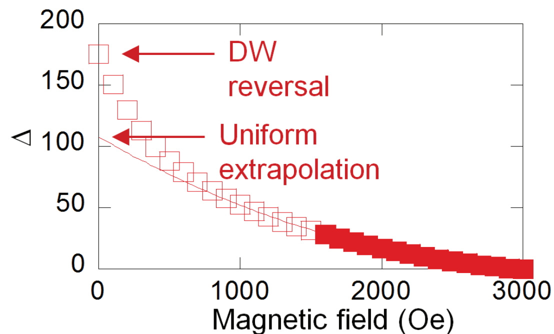

Fig. 11. Comparison of the field dependence of Δ calculated for DW reversal (open symbols) with uniform reversal fit (solid line). Values of Δ accessible experimentally for device-level measurements (Δ~20) are shown as solid symbols.

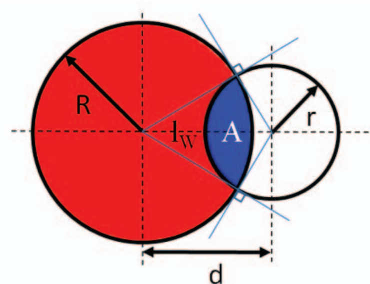

Fig. 12. Schematic of the DW reversal model

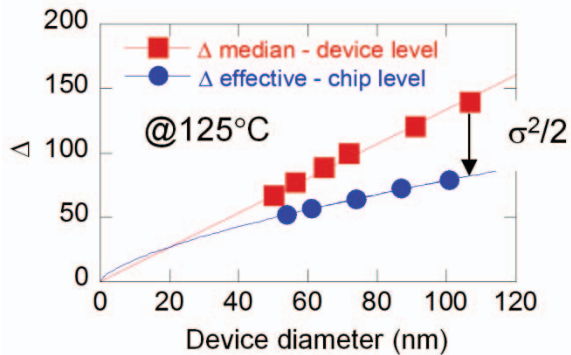

Fig. 13. Comparison of effective and median values of Δ derived at 125°C from chip and device level measurements. Solid lines show fits to a linear and power-law dependence in diameter for Δ median and effective, respectively.

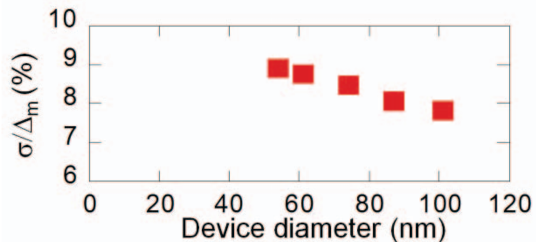

Fig. 14. Width of the distribution of Δ calculated using the expression of Δ_{eff} from the data shown in Figure 13.